Renewable Energy 201 (2022) 678–690

Contents lists available at ScienceDirect

Renewable Energy

journal homepage: www.elsevier.com/locate/renene

Numerical analysis of solar chimney power plant integrated with CH_4 photocatalytic reactors for fighting global warming under ambient crosswind

Hanbing Xiong [a], Tingzhen Ming [a,*], Yongjia Wu [a], Caixia Wang [a], Qiong Chen [a], Wei Li [b], Liwen Mu [c], Renaud de Richter [d], Yanping Yuan [e]

[a] School of Civil Engineering and Architecture, Wuhan University of Technology, Wuhan, 430070, PR China
[b] Institute for Materials and Processes, School of Engineering, The University of Edinburgh, Edinburgh, EH9 3FB, Scotland, UK
[c] College of Chemical Engineering, State Key Laboratory of Materials-oriented Chemical Engineering, Nanjing Tech University, Nanjing, 211816, PR China
[d] Tour-Solaire.Fr, 8 Impasse des Papillons, F34090, Montpellier, France
[e] School of Mechanical Engineering, Southwest Jiaotong University, Chengdu, 610031, PR China

ARTICLE INFO

Keywords:
Solar chimney
Ambient crosswind
Atmospheric CH_4 removal
Photocatalytic reactors
CO_2 emission reduction

ABSTRACT

Methane's global warming potential (GWP) is much larger than carbon dioxide and contributes significantly to global warming. Solar chimney power plant (SCPP) integrated with photocatalytic reactors can capture and remove atmospheric methane, and generate electrical power without fossil energy consumption simultaneously. In this paper, the performance of the flow characteristics, the CH_4 removal, the CO_2 emission reduction, and the power generation were analyzed for the SCPP integrated with different types of photocatalytic reactors under ambient crosswind (ACW). The results revealed that the SCPP integrated with a honeycomb reactor was more stable for the degradation of CH_4 than that with a plate reactor. With an increase in ACW, the removal rate of atmospheric CH_4 was reduced to a constant value of 0.41 g/s for the honeycomb reactor and 0.11 g/s for the plate reactor. The SCPP integrated with a honeycomb reactor achieved a maximum power generation of 88.31 kW, which was 1.63 times than that of the conventional SCPP when $G = 857$ W/m^2 and ACW = 0 m/s. In addition, the improved SCPP could reduce CO_2 emissions by 85.04 kg/h when $G = 857$ W/m^2, ACW = 0 m/s, and $\triangle P = 320$ Pa.

1. Introduction

Since the industrial revolution, the continuous increase in atmospheric CH_4 concentrations was caused by human beings. Despite the fact that the level of CH_4 in the atmosphere is substantially lower than that of CO_2 (1.886 ppm CH_4 vs 417 ppm CO_2), the damage caused by both is comparable [1]. The United Nations Environment Program (UNEP) had long stated that reducing CH_4 emissions could effectively slow the high level of climate change, resulting in global temperature falling by 0.4–0.5 °C by 2050, which would aid in meeting the goal of the Paris Climate Agreement [2–4]. According to a recent report [5,6], it was urgent to limit the increase of the CH_4 concentration in the atmosphere. The level of CH_4 was tightly connected to the rate of global warming for two reasons. Firstly, CH_4 had a considerable radiative forcing impact in a short period. For example, the warming capacity of CH_4 was 120 times than CO_2 of the same mass, and its global warming potential (GWP) was 28–34 times higher even after 100 years [7,8]. Secondly, an increase in global temperatures would release massive amounts of CH_4 locked as gas hydrate on the ocean bottom into the atmosphere, aggravating the greenhouse effect even more [9]. If the atmospheric CH_4 level was reduced to the pre-industrial level (0.76 ppm), a 16% reduction in radiative forcing could be accomplished in approximately 10–20 years [5,10]. Furthermore, even if fossil fuels were abandoned and no new CO_2 was released into the atmosphere, the existing enormous carbon reservoir (513 Gt) of the atmosphere would continue to drive temperature increase and climate change for several decades [11]. Therefore, reducing atmospheric CH_4 is a promising solution to the climate change.

Thermal catalysis was the first suggested method for catalyzing rarefied CH_4, but its applicability was restricted due to high energy consumption, low conversion rate, and easy explosion [12].

* Corresponding author.
E-mail address: tzming@whut.edu.cn (T. Ming).

https://doi.org/10.1016/j.renene.2022.11.024
Received 16 September 2022; Received in revised form 4 November 2022; Accepted 5 November 2022
Available online 7 November 2022

Nomenclature

B, B_1, B_2	Constants for reaction rate of CH_4
$C_{1\varepsilon}$, $C_{2\varepsilon}$	Constants for turbulent model
c_1	CH_4 concentration at inlet of the canopy, $mol{\cdot}m^{-3}$
c_2	O_2 concentration at outlet of the chimney, $mol{\cdot}m^{-3}$
m_1	CH_4 mass fraction at the entrance of reactors
m_2	CH_4 mass fraction at the exit of reactors
r_m	Reaction rate of CH_4 in honeycomb reactor, $mol{\cdot}W^{-1}{\cdot}m^{-1}{\cdot}s^{-1}$
r_{AI}	Reaction rate of CH_4 in plate reactor, $mol{\cdot}W^{-1}{\cdot}s^{-1}$
G	Solar radiation, $W{\cdot}m^{-2}$
q	Heat flux, $W{\cdot}m^{-2}$
SSA	Specific surface area, m^{-1}
$\vec{J_i}$	Diffusion flux of species i, $mol{\cdot}s^{-1}{\cdot}m^{-3}$
Q_m	Mass flow rate, $kg{\cdot}s^{-1}$
$\dot{m}_{CH_4}$	Purification rate of CH_4, $g{\cdot}s^{-1}$
W_e	Output power of system, kW
Δp	Pressure drop of the turbine, Pa
S_Φ	Momentum loss, $N{\cdot}m^{-3}$
S_i	Additional rate, $kg{\cdot}m^{-3}{\cdot}s^{-1}$
C_{eq}	CO_2 equivalent
$\dot{C}_{eq}$	Rate of CO_2 reduction, $kg{\cdot}h^{-1}$

Greek symbols

ν	Kinetic viscosity, $m^2{\cdot}s^{-1}$
β	Coefficient of thermal expansion, K^{-1}
ρ	Gas density, $kg{\cdot}m^{-3}$
τ	Shear stress, $N{\cdot}m^{-2}$
k	Karman Constant

Abbreviations

UNEP	United Nations Environment Program
GWP	Global warming potential
SCPP	Solar chimney power plant
PCRs	Photocatalytic reactors
PPCR	Plate photocatalytic reactor
HPCR	Honeycomb photocatalytic reactor
ACW	Ambient crosswind

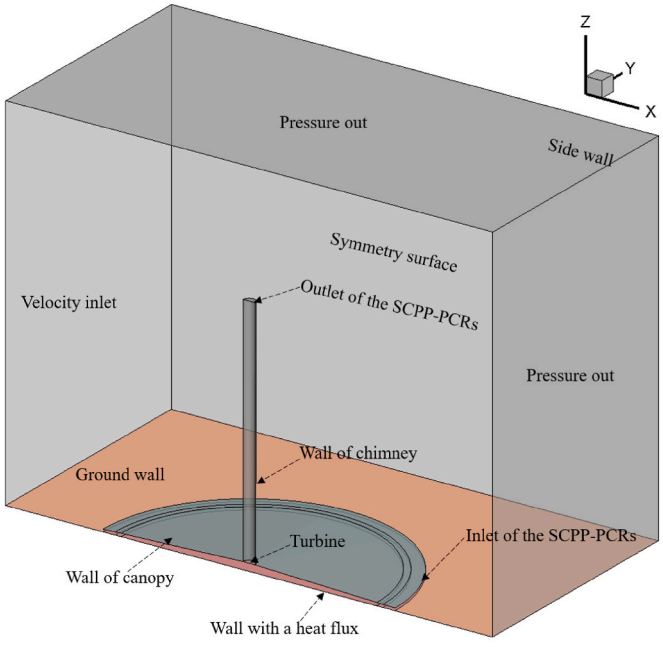

Fig. 1. Schematics of the geometrical model.

Photocatalytic semiconductor technology was a mild and manageable technique of degrading atmospheric CH_4 by employing solar energy, both in terms of energy consumption, safety, and cost [13–15]. There was a dynamic balance between the forward and reverse reactions in the thermocatalytic reaction, whereas, in the photocatalytic reaction, the forward and reverse reaction mechanisms were different, as was the energy. Hence, the photocatalytic reaction can break the thermodynamic balance by eliminating the reverse reaction, which was beneficial to the degradation of CH_4 [16]. Kato et al. [17] adopted Silica-Alumina as a photocatalyst to demonstrate the non-oxidative coupling of CH_4 at room pressure and temperature for the first time, however, the conversion rate was very low (5.9%). The synthesis of new photocatalysts contributed to the improvement of the selectivity and conversion of CH_4 photocatalytic products. Wei et al. [18] reported a photocatalyst using Ga_2O_3 and Activated Carbon (AC) at a mass ratio of 3:17 that performed well. Only CO_2 and H_2O were produced by CH_4 photocatalysis, and the catalytic rate was 91.5% after 2.5 h. Li et al. [19] used a hydrothermal approach to create ZnO nanosheets and nanorods with varying ratios of polar and non-polar crystal faces to focus on the degradation of low-concentration CH_4 (200 ppm). The photocatalytic reaction of CH_4 on the ZnO surface followed quasi-first-order kinetics, with a degradation rate of 80% after 2 h. Other photocatalysts, such as CuO/ZnO [20], Ag/ZnO [21], and $SrCO_3/SrTiO_3$ [22], also exhibited great promise in the degradation of low-concentration CH_4, with conversion rates of up to 100%. Brenneis et al. [23] accomplished all CH_4 removal by passing atmospheric level concentrations of CH_4 (2 ppm–2%) through a reactor containing copper-treated zeolite particles heated to 310 °C. Demonstration projects involving photocatalysis to degrade greenhouse gases were carried out [24–28], but the actual results were unsatisfactory because outdoor environmental factors such as solar radiation, wind speed and direction, and so on had a significant impact on the performance of photocatalysis [29].

The solar chimney power plant (SCPP), a green technology, was firstly proposed and built by Schlaich [30,31], with a maximum power generation of 50 kW. To assess and forecast the performance of the SCPP, a wide range of internal heat transfer models were proposed [32–37]. Computational fluid dynamics (CFD) is a useful tool for numerical simulation of SCPP owing to the rapid advancement of computers. Koonsrisuk et al. [38–40] conducted CFD to investigate the effect of SCPP geometry on flow characteristics inside the system, and the findings revealed that a chimney with a certain divergence angle could improve the output power of the SCPP. Simulation results are more compatible with the actual data by using the radiation and solar load model in commercial software FLUENT [41]. However, due to the limitations of the SCPP prototype of the Spain, such as big floor space and high investment, researchers could only make tiny SCPP for testing. Zhou et al. [42] established a collector with a 10 m diameter and a chimney of 8 m height, and the temperature differential between the collector outlet and the surroundings reached 24.1 °C. Kasaeian et al. [43] in the university of Zanjan built an SCPP. The collector was 10 m in diameter, and the chimney was 13 m in height, made of 12 mm polyethylene tubing. The test data revealed that the collector had a substantial greenhouse effect, the outlet temperature was 25 °C higher than the ambient temperature, and the maximum air speed was 3 m/s. Ghalamchi et al. [44] built a small prototype to study the structural size formula of SCPP and the effect of different storage materials on system

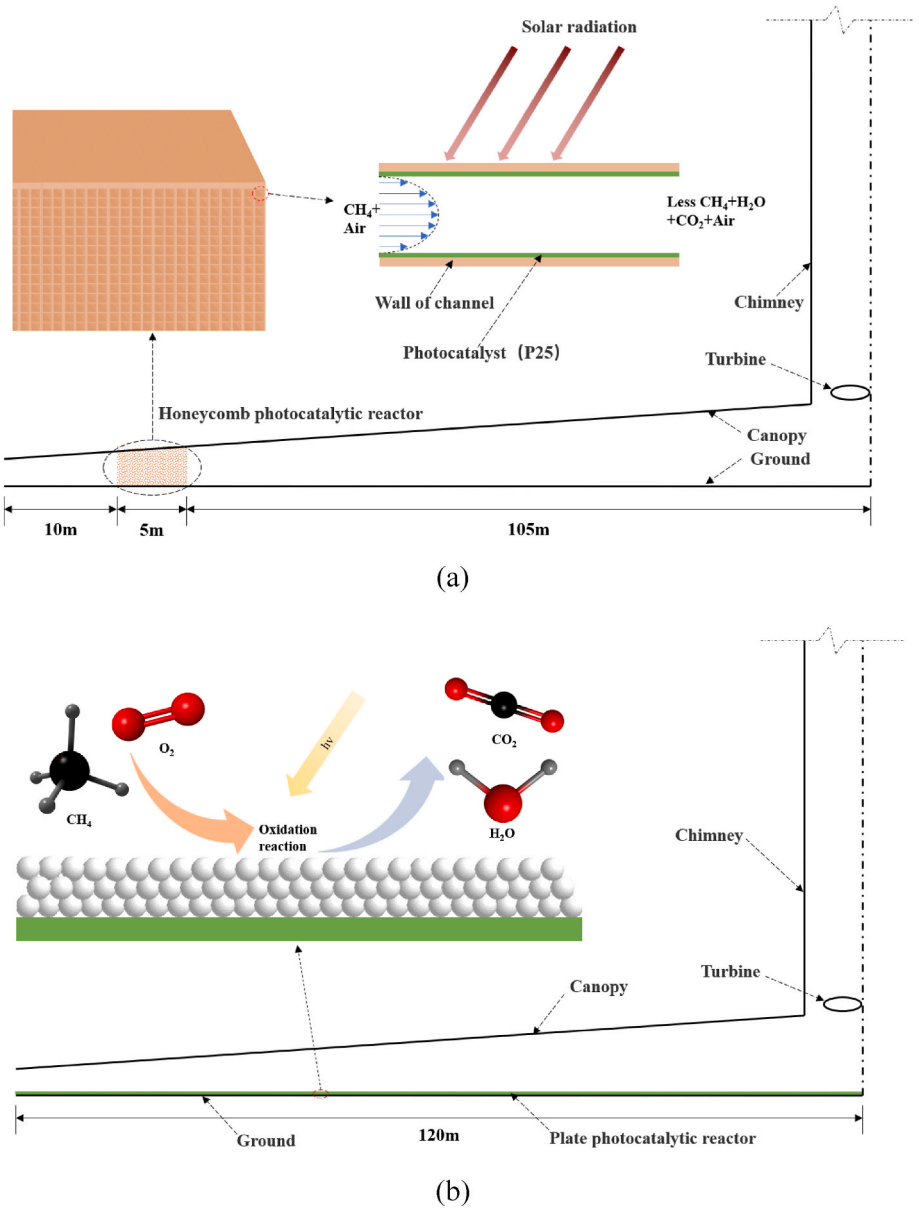

Fig. 2. Schematics of the SCPP-PCRs: (a) SCPP-HPCR; (b) SCPP-PPCR.

performance. Other small prototype trials [45–49] had also been recorded, demonstrating the potential of SCPP.

Innovative studies based on SCPP confirmed promising potential in air pollution purification, saltwater desalination, and crop drying [50,51]. Cao et al. [52] presented a solar-assisted large-scale cleaning system (SALSCS) including a filter bank in the collector that could remove 22.4 km^3/day of urban air pollutants. It could significantly enhance urban air quality. De Richter et al. [53] launched a new concept of SCPP with photocatalytic reactors (SCPP-PCRs) for slowing global warming, where CH_4 was converted to CO_2 and H_2O as airflow moved over the surface of the photocatalyst in the atmosphere. One of the most important factors influencing the capacity of the SCPP-PCRs to degrade atmospheric CH_4 was the type of photocatalytic reactor, such as plate photocatalytic reactor (PPCR) and honeycomb photocatalytic reactor (HPCR) [54]. The reaction area of the HPCR was larger than that of the PPCR, but the pressure drop was higher and the reaction kinetic rate was slower [55,56]. Ming et al. [57,58] used a numerical method to examine the SCPP-PCRs. The atmospheric CH_4 of 21.31 kg per day was degraded, confirming the potential of the SCPP-HPCR for combating climate change. The PPCR just plated a layer of photocatalyst on the ground, with a less impact on the flow characteristics of the system. Another influencing factor was the ambient crosswind (ACW). Serag-eldin [59] briefly analyzed the influence of the ACW on SCPP using the CFD method. Zhou et al. [60] developed a theoretical model to quantitatively evaluate the influence of the ACW at the chimney outlet. Ming et al. [61] demonstrated that when the ACW was relatively weak, the flow field of the SCPP would deteriorate and the performance would degrade, but when the ACW was sufficiently strong, the performance would be improved dramatically. Placing a blockage close to the canopy entry or installing eight radial partition walls within the collector could significantly reduce the adverse impact of the ACW [62,63].

The SCPP-PCRs is a negative emission technology. But research on it is still in its initial stage. Prior research on the SCPP-PCRs assumed that there was no ACW, but the system could not exist in isolation from the environment. It is uncertain how the ACW affects the performance of the photocatalytic CH_4 and power generation after the installation of the HPCR or PPCR. In this paper, the influences of the ACW on the overall performance of the SCPP-PCRs were analyzed by three-dimensional

Table 1
Boundary conditions.

Name and location	Type	Value
Inlet (X = −200 m)	Velocity inlet	$u = \frac{1}{\kappa} \bullet \left(\frac{\tau_s}{\rho}\right)^{\frac{1}{2}} \bullet ln\frac{z}{z_0}$
Outlet (X = 200 m and Z = 300 m)	Pressure outlet	$P = 0$ Pa, $T = 293$ K
Ground below the collector (Z = 0 m)	Heat flux	$q = 600$ W/m^2
Ground beyond the collector (Z = 0 m)	Temperature	$T = 318$ K
Side wall (Y = 200 m)	Wall	$q = 0$ W/m^2
Chimney	Wall	$q = 0$ W/m^2
Turbine	Fan	$\triangle P = 0$–440 Pa
Canopy	Coupling	Exterior surface: $\lambda\left(\frac{\partial T}{\partial x}\right) = \alpha(T_f - T_w)$ Interior surface: $\lambda\left(\frac{\partial T}{\partial x}\right) = \alpha(T_w - T_f)$
Symmetry (Y = 0 m)	Symmetry	$\frac{\partial \varepsilon}{\partial n} = 0$

numerical simulation. This work will help to guide the design and building of the SCPP-PCRs prototype, providing a technical solution for quick and large-scale greenhouse gas removal.

2. Model and method

2.1. Geometric model

The geometric model is determined by simplifying the SCPP Manzanares Prototype in this work [64]. The chimney is 200 m in tall and 10 m in diameter. The collector height increases from 2 m at the entrance to 6 m at the center linearly. And collector diameter is 240 m. Setting acceptable boundary conditions, the performance of SCPP-PCRs in large space can be analyzed by locating the model in the middle of a non-existent box with X, Y, and Z directions of 400 m, 400 m, and 300 m, respectively [61]. Because the model is symmetric at the XZ plane, halving the computational domain, as shown in Fig. 1, does not affect calculation accuracy.

The HPCR is located 10 m from the entrance of the canopy and is 5 m in length, filling the flow channel of the canopy. As indicated in Fig. 2 (a), the photocatalyst (P25) is evenly coated on the inner surface of the honeycomb channel. The honeycomb internal channels are in parallel with the airflow, resulting in relatively low pressure drop. Meanwhile, for the PPCR as shown in Fig. 2(b), the photocatalyst (P25) is uniformly painted on the ground under the collector. The inner environment of SCPP is under negative pressure due to the buoyancy effect caused by solar radiation, thereby, CH_4 in the atmosphere is continually drawn into the system and is converted to CO_2 and H_2O when exposed to the photocatalyst.

2.2. Numerical model

The flow inside the system is driven by the natural convection caused by the solar radiation heating the ground. The Rayleigh number can be used as a criterion to measure the buoyancy force, which is defined by:

$$R_a = \frac{g\beta\Delta T H^3}{av} \tag{1}$$

where ΔT is the maximum temperature rise in the SCPP-PCRs. g, β, a, and H are the gravitational acceleration (9.81 m^2/s), the thermal expansion coefficient, the thermal diffusivity, and the collector height, respectively. The system is in a turbulent state as $R_a > 10^{10}$ [61].

The incompressible ideal gas model is used to model the gas density variation in the SCPP-PCRs [65]. The macroscopical process of CH_4 photocatalytic reaction is simulated using the laminar finite rate model. The governing equations of the flow and chemical reactions in the SCPP-PCRs are given as follows.

$$\frac{\partial(\rho u_i)}{\partial x_i} = 0 \tag{2}$$

$$\frac{\partial(\rho u_i u_j)}{\partial x} = \rho g_i - \frac{\partial p}{\partial x_i} + \frac{\partial \tau_{ij}}{\partial x_j} \tag{3}$$

$$\frac{\partial(\rho c_p u_j T)}{\partial x_j} = \frac{\partial}{\partial x_j}\left(\lambda \frac{\partial T}{\partial x_j}\right) + \tau_{ij}\frac{\partial u_i}{\partial x_j} + \beta T\left(\frac{\partial p}{\partial t} + u_j \frac{\partial p}{\partial x_j}\right) \tag{4}$$

Equation for the turbulent kinetic energy (k):

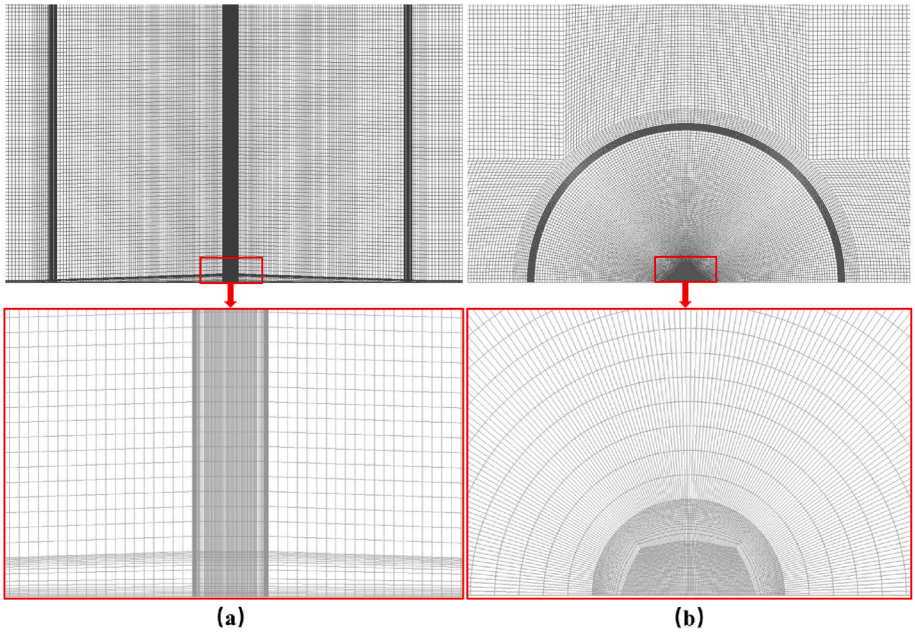

Fig. 3. Grid system of the SCPP-PCRs: (a) grid distribution on the symmetric surface; (b) Top view of grid distribution.

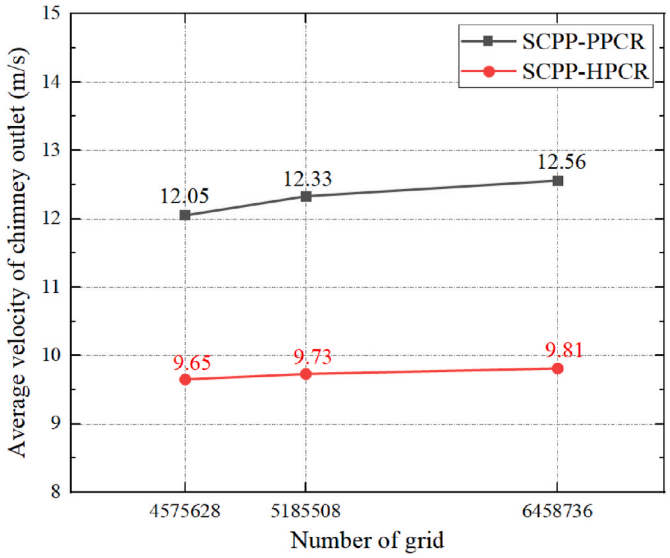

Fig. 4. Grid independence check.

$$\frac{\partial}{\partial x_i}(\rho k u_i) = \frac{\partial}{\partial x_j}\left(\alpha_k \mu_{eff}\frac{\partial k}{\partial x_j}\right) + G_k + G_b - \rho\varepsilon - Y_M + S_k \tag{5}$$

Equation for the energy dissipation (ε):

$$\frac{\partial}{\partial x_i}(\rho \varepsilon u_i) = \frac{\partial}{\partial x_j}\left(\alpha_\varepsilon \mu_{eff}\frac{\partial \varepsilon}{\partial x_j}\right) + C_{1\varepsilon}\frac{\varepsilon}{k}(G_k + C_{3\varepsilon}G_b) - C_{2\varepsilon}\rho\frac{\varepsilon^2}{k} - R_\varepsilon + S_\varepsilon \tag{6}$$

Component transport equation:

$$\nabla \bullet (\rho \vec{v} Y_i) = -\nabla \bullet \vec{J_i} + R_i + S_i \tag{7}$$

where μ_{eff} denotes the effective kinematic viscosity, $\mu_{eff} = \mu + \mu_t$. τ_{ij} is the viscous shear stress, which is $\tau_{ij} = \mu\left(\frac{\partial u_i}{\partial x_j} + \frac{\partial u_j}{\partial x_i}\right)$. G_k represents the generation of turbulence kinetic energy owing to buoyancy, which is defined as $G_k = -\rho\overline{u_i' u_j'}\frac{\partial u_j}{\partial x_i}$, α_k and α_ε are the turbulent Prandtl numbers for k and ε respectively. $\alpha_k = \alpha_\varepsilon = 1.30$. $C_{1\varepsilon}$ and $C_{2\varepsilon}$ are two constants for the turbulent model, with $C_{1\varepsilon} = 1.44$, $C_{2\varepsilon} = 1.92$. $\vec{J_i}$ represents the diffusion flux of species i, $\vec{J_i} = -\rho D_{i,m} + R_i$. R_i represents the amount of component i produced or consumed in a chemical reaction. S_i represents the additional rate owing to the discrete phase. Y_M indicates the variable dilatation incompressible turbulence contribution to the total dissipation rate.

A two-dimensional reverse fan model [66] with a preset pressure drop could calculate the output power of the SCPP-PCRs, with the formula given as follows [67].

$$W_e = \eta_t \bullet \Delta P \bullet V \tag{8}$$

where η_t represents the efficiency of the SCPP-PCRs to convert heat energy into electricity (0.72). ΔP represents a pressure drop. V represents the volume flow rate at the outlet of the SCPP-PCRs.

The reaction rate of CH_4 in the plate reactor is given by [68].

$$r_{AI} = B\frac{B_1 c_1}{1 + B_1 c_1}\frac{B_2 c_2}{1 + B_2 c_2} \tag{9}$$

where c_1 and c_2 are the concentration of CH_4 and O_2, respectively. B, B_1 and B_2 are the associate parameters, whose values are 5.37×10^{-7}, 2.42, and 4.60, respectively.

The honeycomb reactor is simplified as a porous media. The governing equations inside the porous media are presented as follows.

$$\nabla \bullet (\gamma\rho\vec{v}) = 0 \tag{10}$$

$$\nabla \bullet (\gamma\rho\vec{v}) = -\gamma\nabla p(\gamma\vec{\tau}) + \gamma\rho\vec{g} + S_\Phi \tag{11}$$

where γ is porosity ($\gamma = 0.85$), $\vec{\tau}$ represents the viscous stress tensor, S_Φ denotes the momentum loss term, $S_\Phi = -\left(\frac{\mu}{K}\vec{v} + \frac{C}{2}\rho|\vec{v}|\vec{v}\right)$. The permeability ($K$) and the inertia coefficient (C) can be calculated by the Ergun equations [69]:

$$K = \frac{D_P^2}{150}\frac{\gamma^3}{(1-\gamma)^2} \tag{12}$$

$$C = \frac{3.5}{D_P^2}\frac{(1-\gamma)}{\gamma^3} \tag{13}$$

where D_P is the pore diameter.

The reaction rate of CH_4 in the honeycomb reactor is given by

$$r_m = r_{AI} \bullet SSA \tag{14}$$

where SSA is the specific surface area, $SSA = \frac{6(1-\gamma)}{D_P}$ [57].

The purification rate of CH_4 is given by Eq. (15).

$$\dot{m}_{CH_4} = Q_m(m_1 - m_2) \tag{15}$$

where Q_m represents the mass flow rate of the system, m_1 and m_2 are the mass fractions of CH_4 at the entrance and exit of the reactor, respectively.

2.3. Boundary conditions

Fig. 1 shows the boundary conditions and coordinate directions of the model, and the details are listed in Table 1.

Assuming that the ACW measurement at the entrance is completely developed and that the temperature remains constant at 293 K, the wind speed equation at the inlet (X = −200 m) can be fitted using the logarithmic law of atmospheric boundary layer wind speed profile [70]:

$$v = w = 0 \tag{16}$$

$$u = \frac{1}{\kappa} \bullet \left(\frac{\tau_s}{\rho}\right)^{\frac{1}{2}} \bullet ln\frac{z}{z_0} \tag{17}$$

where τ_s is the shear stress on ground surface. z_0 is the aerodynamic roughness length of the ground. κ and z_0 are 0.4 and 0.01, respectively [61].

The ground absorbs solar energy, accounting for 70% of the total amount [61]. When the solar radiation is 857 W/m^2, the heat flux of the ground below the collector is about 600 W/m^2, and other regions are supposed to have a constant temperature boundary (318 K) [62]. The surfaces at X = 200 m and Z = 300 m are two pressure outlets, which are set far enough to ensure the flow field develops fully. The side wall is far from the inlet and outlet of the SCPP-PCRs, therefore the default side wall characteristic parameters are so preserved [62]. The canopy and chimney are set as thermal coupling wall and insulation wall, respectively, and their thickness are neglected.

2.4. Grid system and computational processes

In the process of numerical simulation, the structured grid is more stable and economical than unstructured grid. A hexahedral grid system is used in the model and the generation procedure is carried out with the commercial software ICEM CFD 19.2, as shown in Fig. 3. The SCPP with different photocatalytic reactors employs the same grid system by densifying the grids in the area 10–15 m away from the entrance of the collector. The common fluid region is set for the PPCR and the porous media model is used to simulate the HPCR in this area. Ansys Fluent 19.2 is adopted in the computational procedure. The SIMPLE algorithm is selected for the pressure–velocity coupling scheme. For the pressure

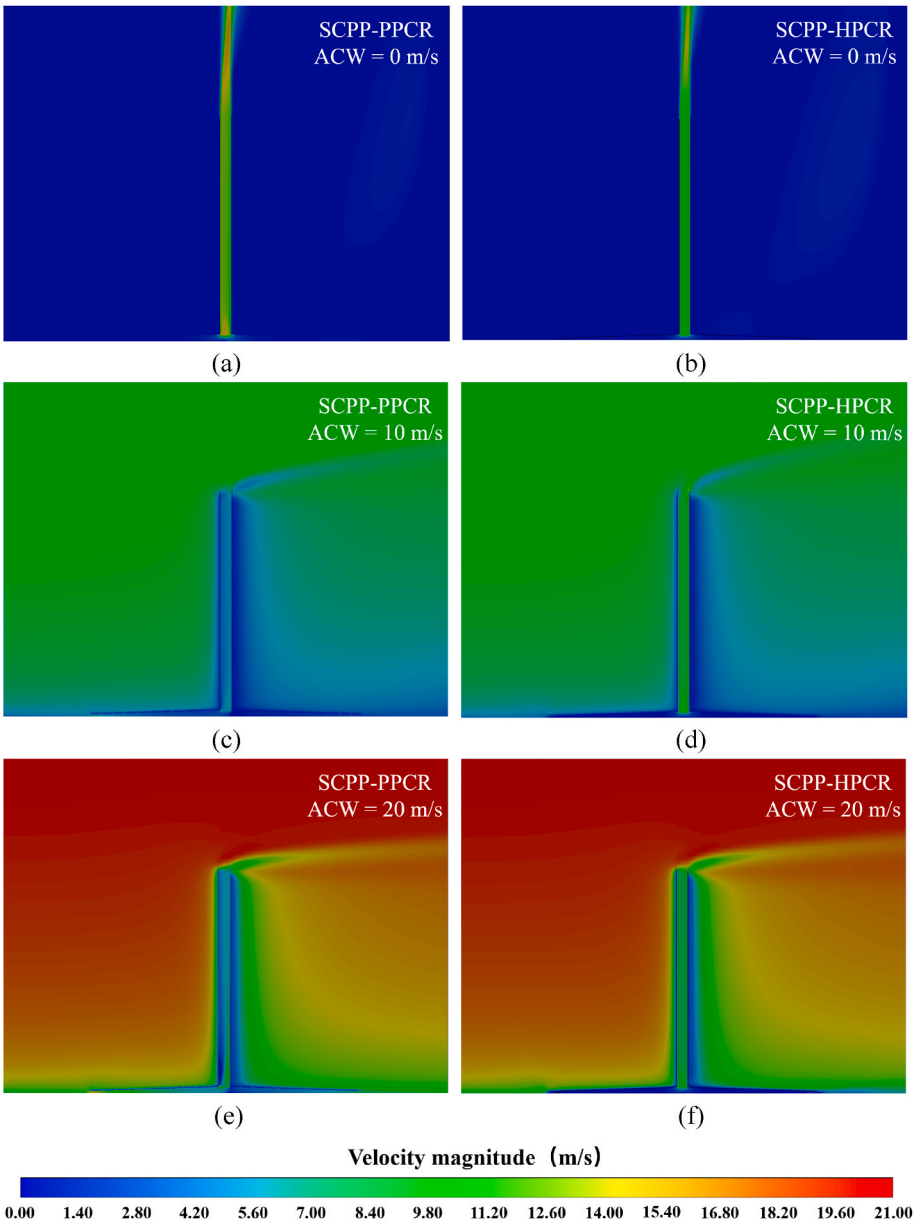

Fig. 5. The velocity contours in the XZ plane (Y = 0 m) of the SCPP-PCRs under ACWs = 0, 10, 20 m/s at G = 857 W/m^2.

term, the PRESTO! divergence scheme is utilized, while the other terms are calculated using the second order upwind scheme. The maximum residuals of all equations are below 10^{-5}. The concentration of CH_4 and the volume flow rate at the chimney outlet remain constant as the criterion for calculating convergence.

Three grid systems with grid numbers of 4,575,628, 5,185,508, and 6,458,736, respectively, are adopted to investigate grid independence. The numerical simulations are carried out in the same conditions (ACW = 0 m/s, G = 857 W/m^2, and $\triangle P$ = 0 Pa). As shown in Fig. 4, The maximum deviation of the average velocity of the chimney outlet is less than 2.32%. Therefore, the simulations are thought grid independent. And the grid system with a grid number of 5,185,508 is adopted for the modeling.

2.5. Simulation validation

For SCPP-PPCR, because the PPCR has minimum affect on the flow of the SCPP, the results are compared with the data in Ref. [71] to confirm the validity of the simulation. The outlet velocity of SCPP-PPCR is 12.33 m/s while that of SCPP is 12.61 m/s when ACW = 0 m/s, G = 857 W/m^2, and $\triangle P$ = 0 Pa. The relative error is 2.22%. For SCPP-HPCR, according to Ref. [57], the outlet velocity of SCPP-HPCR is 9.38 m/s and the purification rate of CH_4 is 0.59 g/s while that of the simulation result are 9.73 m/s and 0.55 g/s when ACW = 0 m/s, G = 857 W/m^2, and $\triangle P$ = 0 Pa. The maximum relative error is 6.78%. As a result, the validation of the simulation is demonstrated as the modeling result matches well with the experimental result.

3. Result and analysis

In this section, a series of the ACWs ($U_{200\ m}$) ranging from 0 to 25 m/s by intervals of 5 m/s were adopted to simulate the effect of the ACW on the performance of the system. The output power of the system was calculated based on the preset turbine pressure drops and the corresponding flow rates [72]. The HPCR was treated as a porous medium with a porosity of 0.85 and a pore size of 4 mm. In addition, the difference in the overall performances of SCPP-PCRs were analyzed under no-load condition.

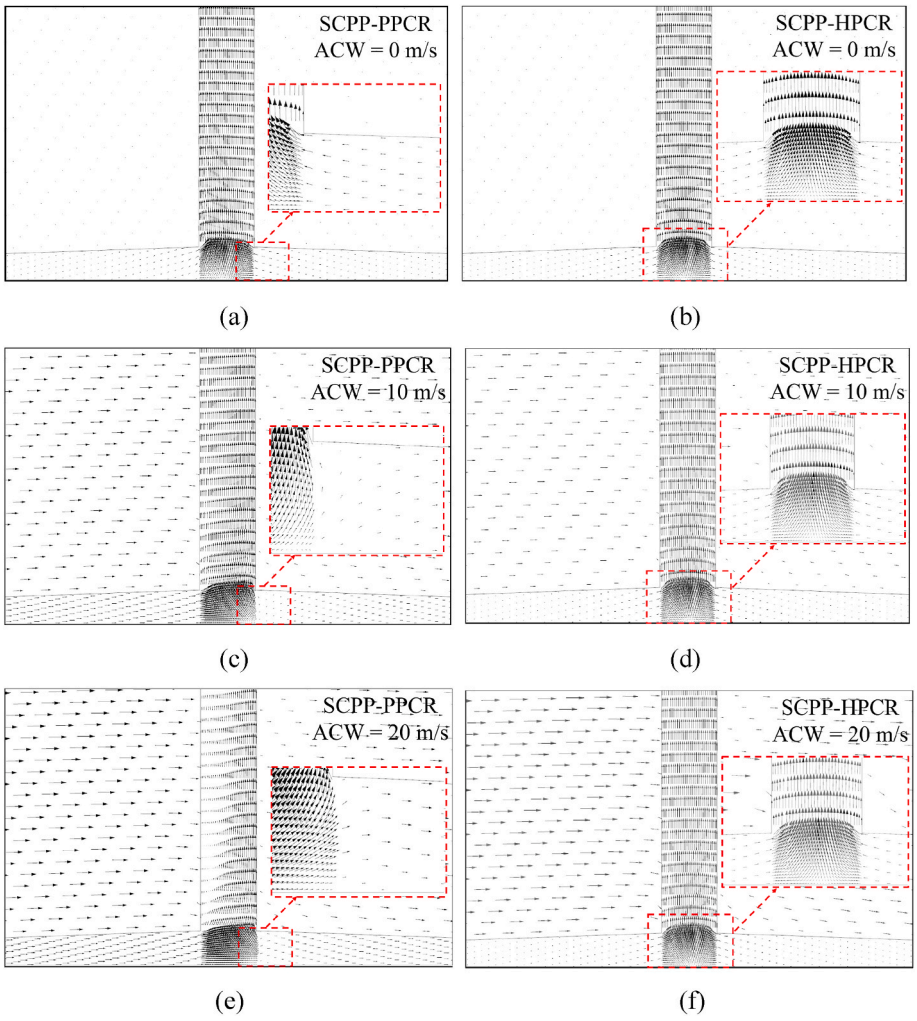

Fig. 6. The velocity vectors at the bottom of the SCPP-PCRs under ACWs = 0, 10, 20 m/s at G = 857 W/m^2.

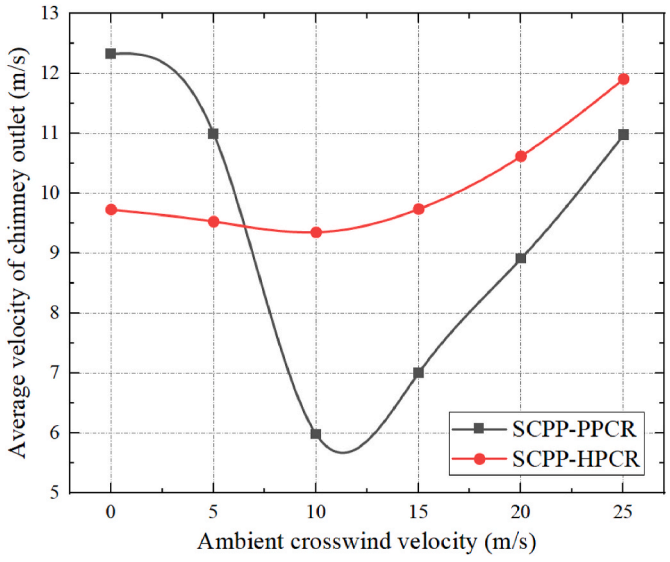

Fig. 7. The average velocity of chimney outlet of the SCPP-PCRs at G = 857 W/m^2.

3.1. Flow characteristics of the SCPP-PCRs

Figs. 5 and 6 showed the contours of velocity in the XZ plane (Y = 0 m) of the SCPP-PCRs under G = 857 W/m^2. Figs. 5 and 6(a), (c), and (e) demonstrated the flow fields of the SCPP with plate photocatalytic reactor (SCPP-PPCR), while Figs. 5 and 6(b), (d), and (f) were the results of the SCPP with honeycomb photocatalytic reactor (SCPP-HPCR). The ACWs were preset to 0 m/s, 10 m/s, and 20 m/s, respectively. As shown in Figs. 5 and 6, the velocity distribution in the two systems were generally symmetrical when ACW = 0 m/s. The SCPP-PPCR had a flow velocity that was higher than the SCPP-HPCR due to the flow resistance caused by the honeycomb reactor.

As shown in Figs. 5 and 6, the HPCR could reduce the impact of the ACWs on the flow in the system. Although the ACW varies, the flow velocity in the SCPP-HPCR were drastically decreased (close to 0 m/s) when the ACW entered the porous material. However, the flow field of the SCPP-PPCR in the collector was significantly impacted by the ACW. The wind coming from the left side of the collector was divided into two streams at the bottom of the chimney, with one flowing into the chimney and another slipping into the right side of the collector.

Fig. 7 showed the average velocity of the chimney outlet of the SCPP-PCRs at G = 857 W/m^2. The outlet velocity of the two systems fluctuated abiding by the same change law, which saw a fall followed by a rise, but the fluctuation ranges differ. When the ACW was weak, the airflow in the collector was collected at the bottom of the chimney. As the porous medium increased the flow resistance, the outlet velocity of the SCPP-

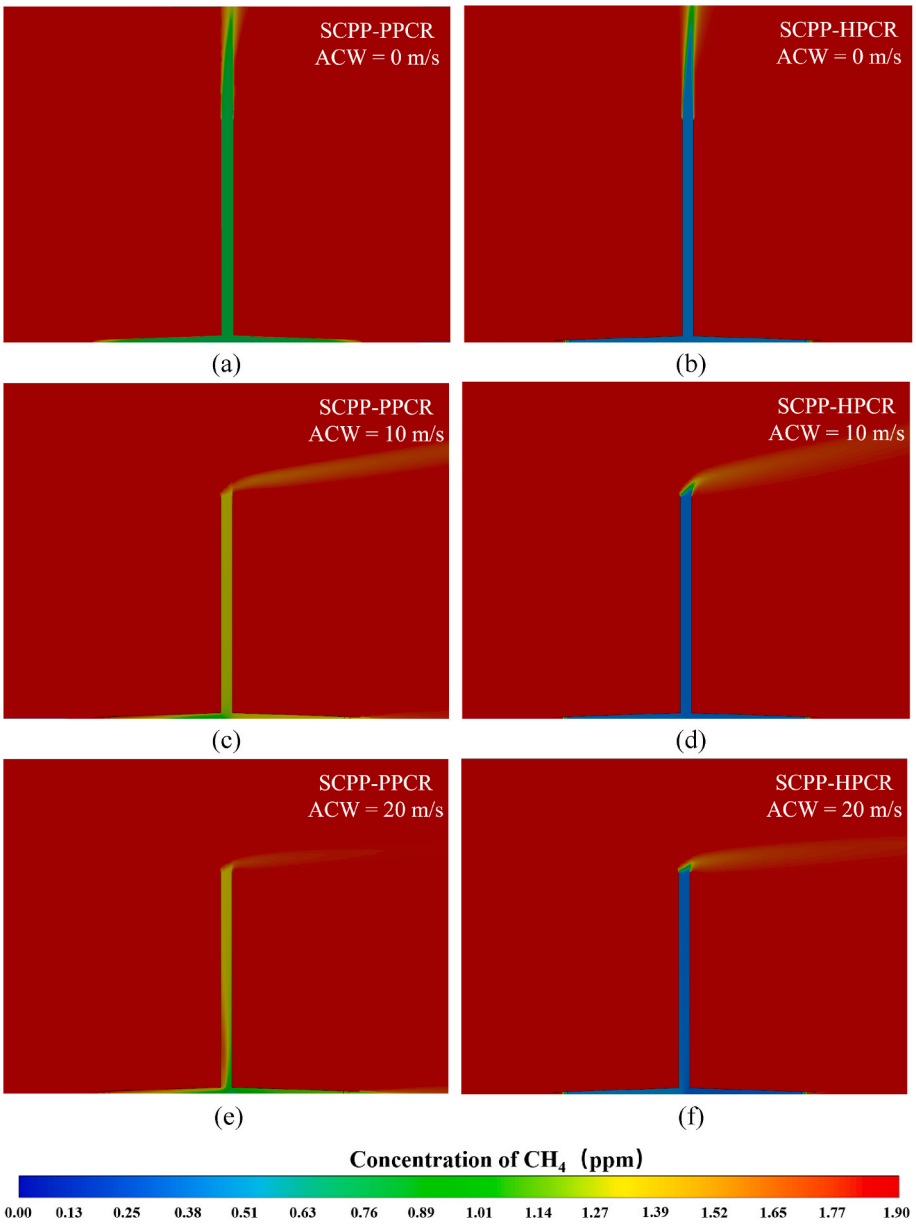

Fig. 8. The contours of CH_4 in the XZ plane (Y = 0 m) of the SCPP-PCRs under ACWs = 0, 10, 20 m/s at G = 857 W/m^2.

PPCR decreased significantly. When ACW = 0 m/s, the outlet velocity of the SCPP-PPCR was 12.33 m/s, while the SCPP-HPCR was only 9.73 m/s. When ACW was larger than 10 m/s, the outlet velocity of the SCPP-PPCR was rapidly decreased due to the enthalpy loss of hot air, which was consistent with the analysis of Serag-Eldin [59]. The outlet velocity of the SCPP-HPCR was slightly reduced due to the resistance of the porous medium, but much higher than that of the SCPP-PPCR. The high-speed air flow at the chimney outlet created a negative pressure zone and strengthens the driving force of the system as the ACW further improves. When the ACW = 15 m/s, the outlet velocity of the SCPP-HPCR reached 9.74 m/s which exceeded that of the ACW = 0 m/s. However, too high ACW could result in forced vibration and static dynamic instability, which could damage the chimney's construction and increase the risk of accidents [73].

3.2. Distribution of CH_4 in the SCPP-PCRs

Fig. 8 showed concentration contours of CH_4 in the XZ plane (Z = 0.01 m) of the SCPPs at G = 857 W/m^2. When the ACW was weak, atmospheric CH_4 entered the system through the collector inlet. Then it was degraded in the reactor. And finally the cleaned air was emitted from the chimney outlet. The stronger the ACW, the faster the CH_4 mixed with the environment at the outlet. In addition, part of atmospheric CH_4 entered the SCPP-PPCR through the entry on the left side of the collector, and flowed into the chimney along the collector without reacting when the ACW was too large (20 m/s) as shown in Fig. 9(e). For the SCPP-HPCR, the distribution of CH_4 in the system was much more uniform and the concentration was lower than that of the SCPP-PPCR.

Fig. 9 displayed the concentration contours of CH_4 in the XY plane (Z = 0.01 m) of the SCPP-PCRs at G = 857 W/m^2. For the SCPP-HPCR, there was a relatively large concentration gradient in the airflow direction as a result of the fast reaction rate in the PPCR. CH_4 escaped to the right from the collector as the ACW continued to strengthen. For the SCPP-HPCR, the concentration of CH_4 decreased in the direction of the reactor when the ACW was weak because it was only degraded in the honeycomb tunnel. The CH_4 in the collector within the reactor was evenly distributed when the ACW was weak. When ACW = 20 m/s, the CH_4 concentration in the collector was lower on the left, because a slight

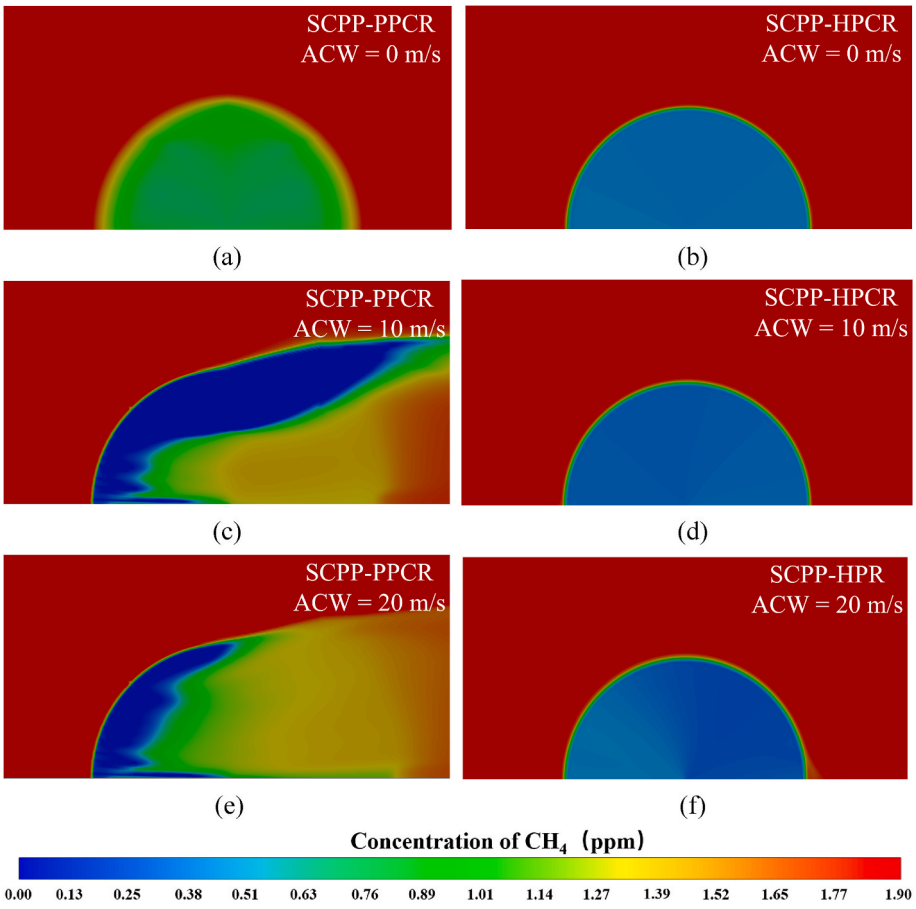

Fig. 9. The distribution of CH_4 in the XY plane (Z = 0.01 m) of the SCPPs under ACWs = 0, 10, 20 m/s at G = 857 W/m^2.

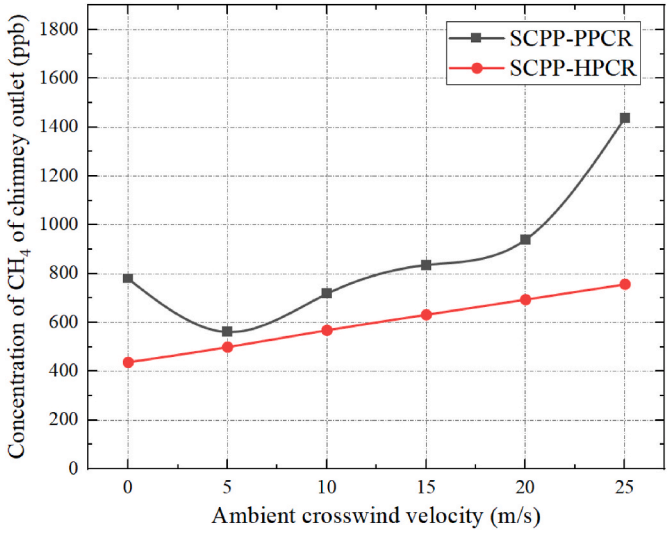

Fig. 10. The concentration of CH_4 in the chimney outlet of the SCPP-PCRs at G = 857 W/m^2.

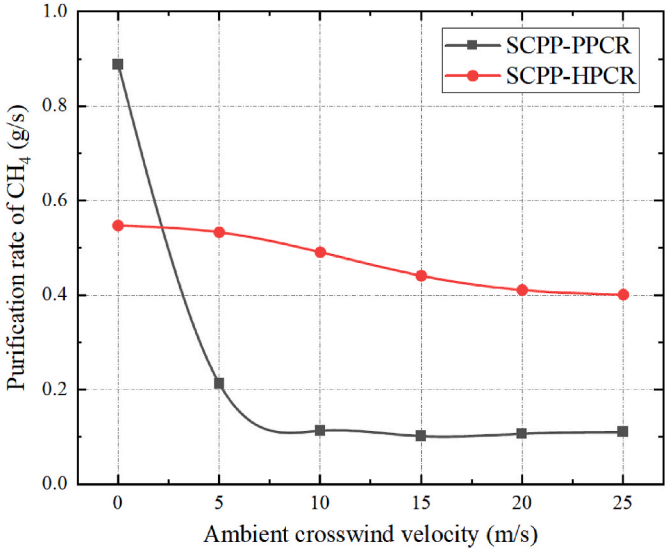

Fig. 11. The CH_4 purification rate of the SCPP-PCRs at G = 857 W/m^2.

leakage of CH_4 occurred at the right inlet of the collector. In general, the removal of atmospheric CH_4 utilizing SCPP-HPCR was easier to control in response to the ACW.

Fig. 10 displayed the concentration contours of CH_4 in the chimney outlet of the SCPP-PCRs at G = 857 W/m^2. The weak ACW inhibited the updraft at the chimney outlet of the SCPP-PPCR [61], resulting in slower airflow and a longer time for CH_4 to react when the ACW = 5 m/s. As a result, the concentration of CH_4 at the outlet decreased. When ACW was strong, atmospheric CH_4 entered the chimney along the collector's interior wall without reacting. Additionally, an amount of cleaned air was to escape out of the right side of the collector, resulting in a high concentration of CH_4 at the outlet of the chimney. The concentration of CH_4 at the exit for the SCPP-HPCR rose linearly with the ACW, and it was lower than the SCPP-PPCR. The CH_4 concentration of the outlet at

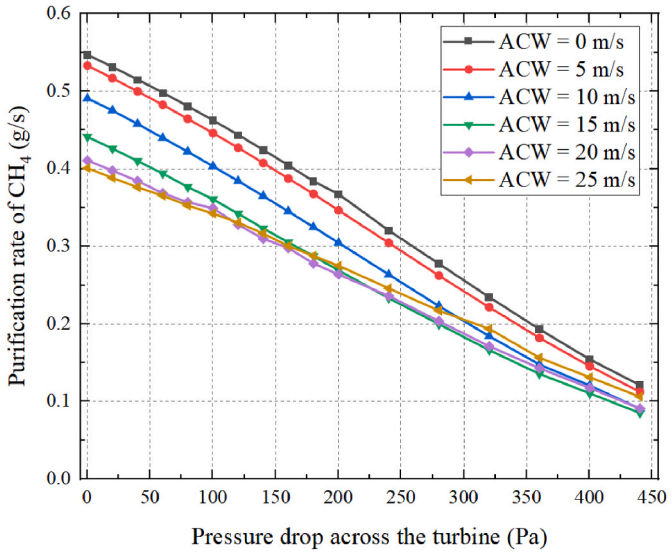

Fig. 12. The performance of CH_4 degradation of the SCPP-HPCR at $G = 857$ W/m^2.

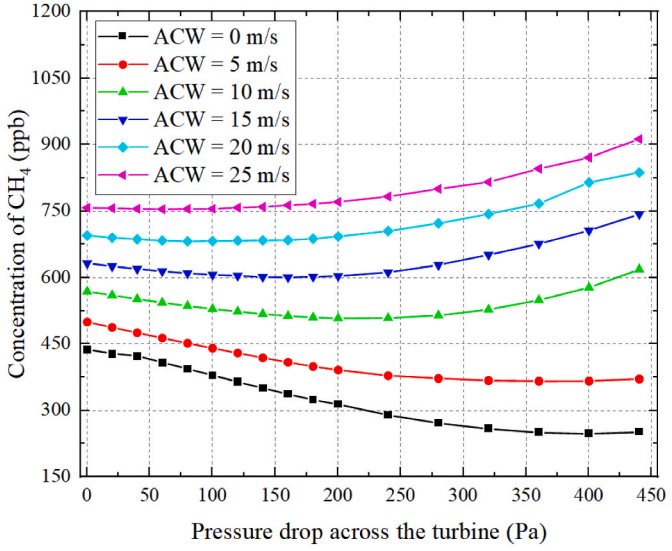

Fig. 13. The concentration of CH_4 in the outlet of the SCPP-HPCR at $G = 857$ W/m^2.

757.51 ppb was roughly half that of the SCPP-PPCR when the ACW = 25 m/s.

3.3. Performance of methane degradation

Fig. 11 displayed the CH_4 purification rate of the SCPP-PCRs at $G = 857$ W/m^2. The purification rate of CH_4 for the two systems steadily dropped with an increase in ACW, eventually approaching a constant value. As seen in Figs. 7 and 10, when the ACW = 0 m/s, the SCPP-PPCR had a higher outlet flow rate than the SCPP-HPP, but the concentration of CH_4 was higher. However, the purification rate of CH_4 of the SCPP-PPCR at 0.89 g/s was higher than the SCPP-HPCR of 0.54 g/s as demonstrated in Fig. 11. Therefore, the flow rate of the outlet of the system was extremely important for the purification rate of CH_4. When the ACW = 10 m/s, the SCPP-PPCR tend to purify CH_4 at a rate of 0.11 g/s that did not drop when ACW increases, but the SCPP-HPCR was 0.41 g/s under the ACW = 25 m/s.

It was found that the SCPP-HPCR was better at purifying atmospheric

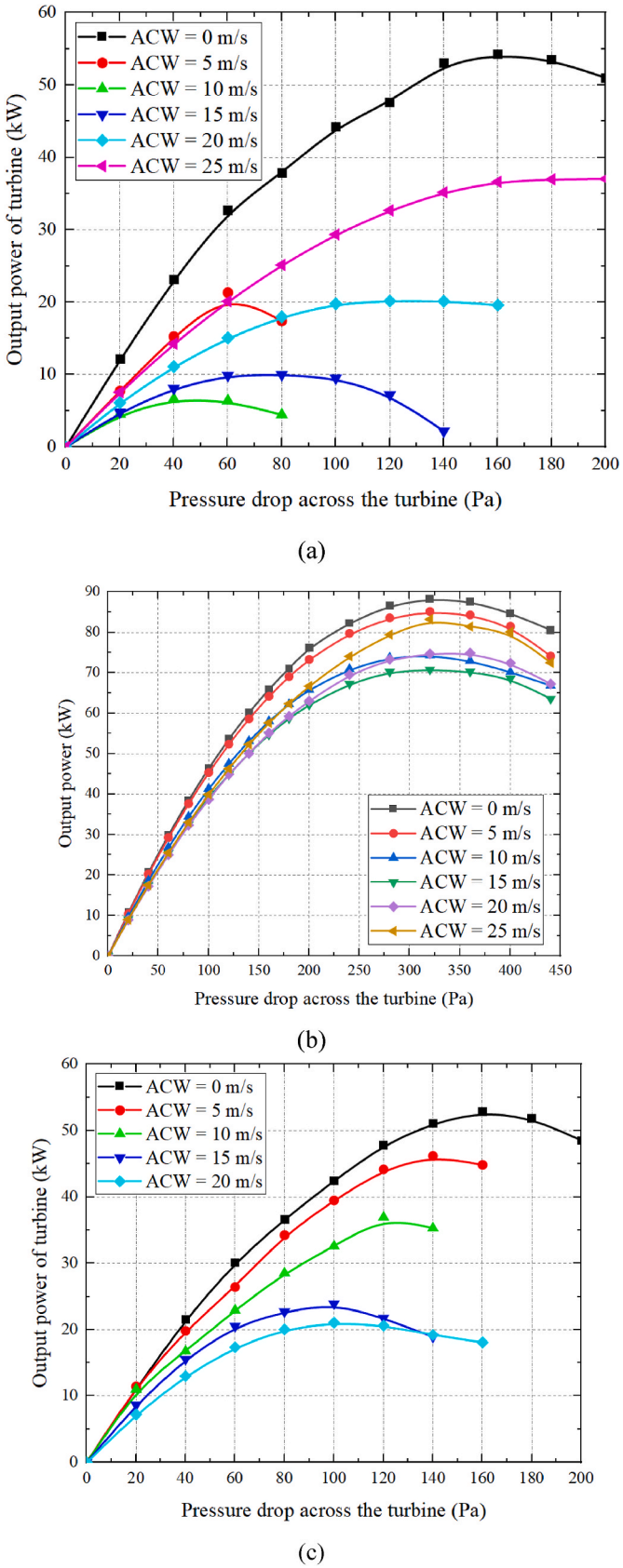

Fig. 14. The output power of the SCPP with different structures at $G = 857$ W/m^2: (a) SCPP-PPCR; (b) SCPP-HPCR; (c) SCPP with blockage [62].

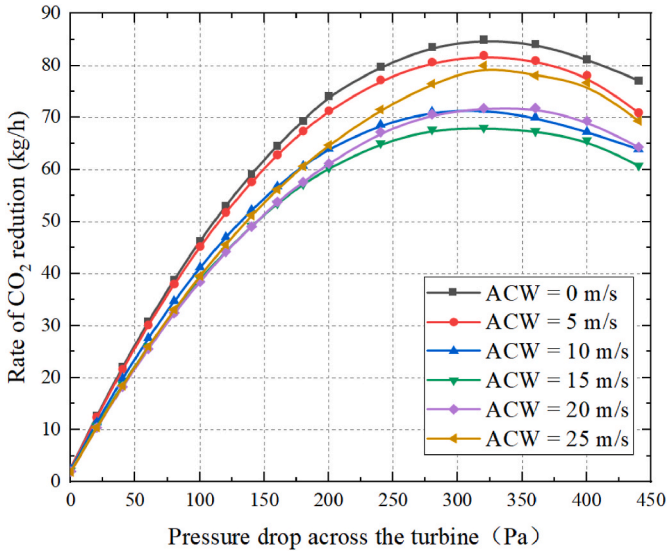

Fig. 15. The rate of CO_2 reduction of the SCPP-HPCR at $G = 857$ W/m^2.

CH_4 than the SCPP-PPCR. The association between the purification rate of CH_4 and turbine pressure drop of the SCPP-HPCR was discussed.

Fig. 12 displayed the CH_4 degradation performance of the SCPP-HPCR at $G = 857$ W/m^2. More kinetic energy from the thermal flow in the system was turned into the mechanical energy of the turbine. The output power of the turbine could increase, but the mass flow rate of the system was significantly decreased. The purification rate of CH_4 was greatly influenced by the mass flow rate of the system, hence purification rate fell as the pressure drop of the turbine increased. It was worth noting that the downward trend of CH_4 purification rate became slow when the ACW = 20 and 25 m/s. The purification rate was higher than in the case of relatively weak ACW as turbine pressure drop increased. This was due to the outlet velocity of the chimney was higher at the ACW = 20 and 25 m/s, as shown in Fig. 7.

Fig. 13 displayed the concentration of CH_4 in the outlet of the SCPP-HPCR at $G = 857$ W/m^2. When the pressure drop of the turbine increased, the concentration of CH_4 at the chimney outlet could reach a minimal value, but the stronger the ACW, the higher the CH_4 concentration at the chimney outlet. For example, the level of CH_4 at the chimney outlet was 247.49 ppb when the ACW = 0 m/s and the $\triangle P$ = 400 Pa, but the level of CH_4 was 754.47 ppb when the ACW = 25 m/s and the $\triangle P$ = 60 Pa.

3.4. SCPP-PPCR structure optimization

In the case of kilowatt-level SCPP, placing a blockage close to the collector entrance could diminish the adverse effects of ACW on the collector entrance but not on the chimney outlet [62]. The impact of the ACW on the output power of SCPP-PPCR and SCPP-HPCR, and SCPP with a blockage was shown in Fig. 14.

Regardless of the structures, the output power of the system was always at its maximum when the ACW = 0 m/s. The maximum output power of the SCPP-HPCR was more than that of the other two structures, and the corresponding turbine pressure drop also increased. For instance, when the ACW = 0 m/s, the maximum output power of the SCPP-PPCR was 54.23 kW, the SCPP with a blockage was 52.85 kW, and the SCPP-HPCR was 88.31 kW. Therefore, the SCPP-PPCR could optimize the structure of the SCPP to improve the power generation performance, which was 1.63 times that of SCPP and 1.67 times that of SCPP with a blockage. In addition, an excessive turbine pressure drop during the numerical computation procedure would make the solver unstable and eventually caused the calculation to diverge.

3.5. Carbon dioxide emission reduction analysis

The carbon dioxide equivalent (C_{eq}) was a parameter to evaluate the total greenhouse effect. The non-CO_2 greenhouse gas emissions were converted into CO_2 emissions [74] by the following formula.

$$C_{eq} = \sum_{i=1}^{n} Q_i \times GWP_i \tag{18}$$

where Q_i was the emission of greenhouse gas i.

The CH_4 had a GWP value of 84 during the first 20 years after the emission, therefore one ton of CH_4 removal was equal to 84 tons of CO_2 emission reduction [53]. The main source of electricity in most countries was thermal power generation. But the burning of fossil fuels would emit a large amount of CO_2 into the atmosphere. It was reported that 0.95 kg of CO_2 was typically released every 1 kW-h of generation by a coal-fired power station [75]. The SCPP-PCRs could achieve CO_2 reduction and obtain clean power without harming the environment. In addition, the system degraded atmospheric CH_4 and produced equimolar CO_2. Consequently, the CO_2 reduction rate of the SCPP-PCRs was as follows:

$$\dot{C}_{eq} = \dot{m}_{CH_4} \times 84 + \dot{m}1_{CO_2} - \dot{m}2_{CO_2} \tag{19}$$

where $\dot{m}_{CH_4}$ represented the purification rate of CH_4, $\dot{m}1_{CO_2}$ represented the reduction rate of CO_2 emission from coal-fired power station, $\dot{m}2_{CO_2}$ represented the generation rate of CO_2 from photocatalytic CH_4.

Fig. 15 showed the CO_2 emission reduction rate of the SCPP-HPCR at $G = 857$ W/m^2. The CO_2 emission reduction of the SCPP-HPCR could reach 85.04 kg/h when $G = 857$ W/m^2 and $\triangle P = 320$ Pa. The usage life of SCPP was between 80 and 120 years [76]. Considering the SCPP's building costs, the returns was produced after just 15 to 40 runs [77]. Furthermore, the P25 was a stable photocatalyst with long life [78]. If the SCPP-HPCRs were implemented, the economically efficient would be improved because of increased electricity generation, and CH_4 was degraded on a large scale to achieve the goal of mitigating climate change.

4. Conclusion

The SCPP-PCRs had enormous promise for combating climate change, but its ability to degrade CH_4 in open spaces was unclear. A comprehensive numerical analysis was conducted for the SCPPs to study the potential using SCPP for atmospheric CH_4 removal under the ACW. The conclusions were drawn as follows.

(1) In comparison to the SCPP-PPCR, the SCPP-HPCR could significantly improve the heat collection performance under ACW conditions.
(2) For the SCPP-PPCR, part of purified air escaped from the collector under the strong ACW conditions, but the SCPP-HPCR appeared to be more stable and controllable in CH_4 degradation.
(3) The mass flow rate significantly impacted on the rate of CH_4 decomposition. When ACW = 0 m/s, the SCPP-PPCR degraded CH_4 at a rate of 0.89 g/s compared to SCPP-HPCR's 0.54 g/s. The degradation rate of CH_4 of SCPP-PPCR reduced quickly and then stabilizes at 0.11 g/s when the ACW increases, whereas the rate of the SCPP-HPCR declined gradually and stabilizes at 0.41 g/s.
(4) The maximum power generation of SCPP-HPCR was 1.63 times that of SCPP and 1.67 times that of SCPP with a blockage. And the CO_2 emission reduction could reach 85.04 kg/h when $G = 857$ W/m^2, ACW = 0 m/s, and $\triangle P = 320$ Pa for a single SCPP-HPCR.

CRediT authorship contribution statement

Hanbing Xiong: Investigation, Software, Methodology, Writing – original draft, preparation. **Tingzhen Ming:** Supervision,

Conceptualization, Software, Resources. **Yongjia Wu:** Writing - Review, Visualization. **Caixia Wang:** Writing – review & editing, Visualization. **Qiong Chen:** Writing – review & editing, Investigation. **Wei Li:** Software, Writing – review & editing, Investigation. **Liwen Mu:** Writing - Review, Visualization. **Renaud de Richter:** Supervision, Visualization, Validation. **Yanping Yuan:** Writing - Review, Visualization.

Declaration of competing interest

The authors declare that they have no known competing financial interests or personal relationships that could have appeared to influence the work reported in this paper.

Acknowledgments

This research was supported by the National Key Research and Development Plan (Grant No. 2019YFE0197500), the European Commission H2020 Marie Curie Research and Innovation Staff Exchange (RISE) award (Grant No. 871998), and the National Natural Science Foundation of China (Grant No. 52278123).

References

[1] M. Saunois, R. Jackson, P. Bousquet, B. Poulter, J. Canadell, The growing role of methane in anthropogenic climate change, Environ. Res. Lett. 11 (12) (2016), 120207.
[2] L. Berrang-Ford, J.D. Ford, J. Amann, Are we adapting to climate change? Global Environ. Change 21 (1) (2011) 25–33.
[3] K. Blok, W. Hare, N. Hohne, M. Kainuma, J. Kejun, D.S. Lee, J. Rogelj, A. Shukla, D. Arent, J. Bogner, Bridging the Emissions Gap: A UNEP Synthesis Report, United Nations Environment Programme (UNEP), 2011.
[4] N. Mengis, H.D. Matthews, Non-CO2 forcing changes will likely decrease the remaining carbon budget for 1.5 degrees C, Npj Clim. Atmos. Sci. 3 (1) (2020) 1–7.
[5] J.C. Kuylenstierna, E. Michalopoulou, C. Malley, Global Methane Assessment: Benefits and Costs of Mitigating Methane Emissions, 2021.
[6] R.P. Allan, E. Hawkins, N. Bellouin, B. Collins, IPCC, 2021, Summary for Policymakers, 2021.
[7] R.K. Pachauri, M.R. Allen, V.R. Barros, J. Broome, W. Cramer, R. Christ, J.A. Church, L. Clarke, Q. Dahe, P. Dasgupta, Climate Change 2014: Synthesis Report. Contribution of Working Groups I, II and III to the Fifth Assessment Report of the Intergovernmental Panel on Climate Change, Ipcc2014.
[8] T. Stocker, Climate Change 2013: the Physical Science Basis: Working Group I Contribution to the Fifth Assessment Report of the Intergovernmental Panel on Climate Change, Cambridge university press2014.
[9] K. Kretschmer, A. Biastoch, L. Ruepke, E. Burwicz, Modeling the fate of methane hydrates under global warming, Global Biogeochem. Cycles 29 (5) (2015) 610–625.
[10] R. Jackson, E. Solomon, J. Canadell, M. Cargnello, C. Field, Methane removal and atmospheric restoration, Nat. Sustain. 2 (6) (2019) 436–438.
[11] H.D. Matthews, K. Caldeira, Stabilizing climate requires near-zero emissions, Geophys. Res. Lett. 35 (4) (2008).
[12] A.E. Shilov, G.B. Shul'pin, Activation of C– H bonds by metal complexes, Chem. Rev. 97 (8) (1997) 2879–2932.
[13] R.P. Noceti, C.E. Taylor, J.R. D'Este, Photocatalytic conversion of methane, Catal. Today 33 (1–3) (1997) 199–204.
[14] C.F. Lien, M.T. Chen, Y.F. Lin, J.L. Lin, Photooxidation of methane over TiO2, J. Chin. Chem. Soc. 51 (1) (2004) 37–42.
[15] T. Ming, W. Li, Q. Yuan, P. Davies, R. de Richter, C. Peng, Q. Deng, Y. Yuan, S. Caillol, N. Zhou, Perspectives on removal of atmospheric methane, Adv. Appl. Energy 5 (2022), 100085.
[16] L. Yuliati, T. Hattori, H. Itoh, H. Yoshida, Photocatalytic nonoxidative coupling of methane on gallium oxide and silica-supported gallium oxide, J. Catal. 257 (2) (2008) 396–402.
[17] Y. Kato, H. Yoshida, T. Hattori, Photoinduced non-oxidative coupling of methane over silica-alumina and alumina around room temperature, Chem. Commun. (21) (1998) 2389–2390.
[18] J. Wei, J. Yang, Z. Wen, J. Dai, Y. Li, B. Yao, Efficient photocatalytic oxidation of methane over β-Ga2O3/activated carbon composites, RSC Adv. 7 (60) (2017) 37508–37521.
[19] Z.H. Li, M.A. Boda, X.Y. Pan, Z.G. Yi, Photocatalytic oxidation of small molecular hydrocarbons over ZnO nanostructures: the difference between methane and ethylene and the impact of polar and nonpolar facets, ACS Sustain. Chem. Eng. 7 (23) (2019) 19042–19049.
[20] Z. Li, X. Pan, Z. Yi, Photocatalytic oxidation of methane over CuO-decorated ZnO nanocatalysts, J. Mater. Chem. 7 (2) (2019) 469–475.
[21] X. Chen, Y. Li, X. Pan, D. Cortie, X. Huang, Z. Yi, Photocatalytic oxidation of methane over silver decorated zinc oxide nanocatalysts, Nat. Commun. 7 (1) (2016) 1–8.
[22] X. Pan, X. Chen, Z. Yi, Photocatalytic oxidation of methane over SrCO 3 decorated SrTiO 3 nanocatalysts via a synergistic effect, Phys. Chem. Chem. Phys. 18 (46) (2016) 31400–31409.
[23] R.J. Brenneis, E.P. Johnson, W. Shi, D.L. Plata, Atmospheric- and Low-Level Methane Abatement via an Earth-Abundant Catalyst, ACS Environmental Au, 2021.
[24] H. Dylla, M.M. Hassan, D. Osborn, Field evaluation of ability of photocatalytic concrete pavements to remove nitrogen oxides, transportation research record, J. Transport. Res. Board 2290 (1) (2012) 154–160.
[25] G.L. Guerrini, Photocatalytic performances in a city tunnel in Rome: NOx monitoring results, Construct. Build. Mater. 27 (1) (2012) 165–175.
[26] M. Gallus, V. Akylas, F. Barmpas, A. Beeldens, E. Boonen, A. Boréave, M. Cazaunau, H. Chen, V. Daële, J. Doussin, Photocatalytic de-pollution in the Leopold II tunnel in Brussels: NOx abatement results, Build. Environ. 84 (2015) 125–133.
[27] M. Gallus, R. Ciuraru, F. Mothes, V. Akylas, F. Barmpas, A. Beeldens, F. Bernard, E. Boonen, A. Boréave, M. Cazaunau, Photocatalytic abatement results from a model street canyon, Environ. Sci. Pollut. Control Ser. 22 (22) (2015) 18185–18196.
[28] E. Boonen, V. Akylas, F. Barmpas, A. Boréave, L. Bottalico, M. Cazaunau, H. Chen, V. Daële, T. De Marco, J. Doussin, Construction of a photocatalytic de-polluting field site in the Leopold II tunnel in Brussels, J. Environ. Manag. 155 (2015) 136–144.
[29] H. Dylla, M.M. Hassan, D. Osborn, Field evaluation of ability of photocatalytic concrete pavements to remove nitrogen oxides, Transport. Res. Rec. 2290 (2290) (2012) 154–160.
[30] W. Haaf, K. Friedrich, G. Mayr, J. Schlaich, Solar chimneys Part I: principle and construction of the pilot plant in manzanares, Int. J. Sol. Energy 2 (1) (2007) 3–20.
[31] W. Haaf, Solar chimneys, Int. J. Sol. Energy 2 (2) (2007) 141–161.
[32] N. Pasumarthi, S. Sherif, Experimental and theoretical performance of a demonstration solar chimney model—Part I: mathematical model development, Int. J. Energy Res. 22 (3) (1998) 277–288.
[33] N. Pasumarthi, S. Sherif, Experimental and theoretical performance of a demonstration solar chimney model—Part II: experimental and theoretical results and economic analysis, Int. J. Energy Res. 22 (5) (1998) 443–461.
[34] X.P. Zhou, F. Wang, J.A. Fan, R.M. Ochieng, Performance of solar chimney power plant in Qinghai-Tibet Plateau, Renew. Sustain. Energy Rev. 14 (8) (2010) 2249–2255.
[35] X.P. Zhou, S. Yuan, M.A.D. Bernardes, Sloped-collector solar updraft tower power plant performance, Int. J. Heat Mass Tran. 66 (2013) 798–807.
[36] Z. Akhtar, K.V.S. Rao, Theoretical performance analysis of solar chimney power plant for kota region of Rajasthan, India, Appl. Mech. Mater. 787 (2015) 157–161.
[37] M.A.D. Bernardes, A. Voss, G. Weinrebe, Thermal and technical analyses of solar chimneys, Sol. Energy 75 (6) (2003) 511–524.
[38] A. Koonsrisuk, Comparison of conventional solar chimney power plants and sloped solar chimney power plants using second law analysis, Sol. Energy 98 (2013) 78–84.
[39] A. Koonsrisuk, Mathematical modeling of sloped solar chimney power plants, Energy 47 (1) (2012) 582–589.
[40] A. Koonsrisuk, T. Chitsomboon, Partial geometric similarity for solar chimney power plant modeling, Sol. Energy 83 (9) (2009) 1611–1618.
[41] P.-h. Guo, J.-y. Li, Y. Wang, Numerical simulations of solar chimney power plant with radiation model, Renew. Energy 62 (2014) 24–30.
[42] X.P. Zhou, J.K. Yang, B. Xiao, G.X. Hou, Experimental study of temperature field in a solar chimney power setup, Appl. Therm. Eng. 27 (11–12) (2007) 2044–2050.
[43] A.B. Kasaeian, E. Heidari, S.N. Vatan, Experimental investigation of climatic effects on the efficiency of a solar chimney pilot power plant, Renew. Sustain. Energy Rev. 15 (9) (2011) 5202–5206.
[44] M. Ghalamchi, A. Kasaeian, M. Ghalamchi, A.H. Mirzahosseini, An experimental study on the thermal performance of a solar chimney with different dimensional parameters, Renew. Energy 91 (Jun) (2016) 477–483.
[45] N. Pasumarthi, S.A. Sherif, Experimental and theoretical performance of a demonstration solar chimney model - Part II: experimental and theoretical results and economic analysis, Int. J. Energy Res. 22 (5) (1998) 443–461.
[46] C. Ketlogetswe, J.K. Fiszdon, O.O. Seabe, RETRACTED: solar chimney power generation project—the case for Botswana, Renew. Sustain. Energy Rev. 12 (7) (2008) 2005–2012.
[47] S. Kalash, W. Naimeh, S. Ajib, Experimental investigation of the solar collector temperature field of a sloped solar updraft power plant prototype, Sol. Energy 98 (2013) 70–77.
[48] A. Kasaeian, M. Ghalamchi, M. Ghalamchi, Simulation and optimization of geometric parameters of a solar chimney in Tehran, Energy Convers. Manag. 83 (2014) 28–34.
[49] O.K. Ahmed, A.S. Hussein, New design of solar chimney (case study), Case Stud. Therm. Eng. 11 (2018) 105–112.
[50] A.G. Ferreira, C.B. Maia, M.F.B. Cortez, R.M. Valle, Technical feasibility assessment of a solar chimney for food drying, Sol. Energy 82 (3) (2008) 198–205.
[51] L. Zuo, Z.H. Liu, L. Ding, N. Qu, P.Z. Dai, B.F. Xu, Y. Yuan, Performance analysis of a wind supercharging solar chimney power plant combined with thermal plant for power and freshwater generation, Energy Convers. Manag. 204 (2020).
[52] Q. Cao, D.Y. Pui, W. Lipinski, A concept of a novel solar-assisted large-scale cleaning system (SALSCS) for urban air remediation, Aerosol Air Qual. Res. 15 (1) (2015) 1–10.
[53] R. de Richter, T.Z. Ming, P. Davies, W. Liu, S. Caillol, Removal of non-CO2 greenhouse gases by large-scale atmospheric solar photocatalysis, Prog. Energ Combust. 60 (2017) 68–96.

[54] O.M. Alfano, A.E. Cassano, Scaling-up of photoreactors: applications to advanced oxidation processes, Adv. Chem. Eng. 36 (2009) 229–287.
[55] M.M. Hossain, G.B. Raupp, S.O. Hay, T.N. Obee, Three-dimensional developing flow model for photocatalytic monolith reactors, AIChE J. 45 (6) (1999) 1309–1321.
[56] R. Yang, Y. Zhang, Q. Xu, J. Mo, A mass transfer based method for measuring the reaction coefficients of a photocatalyst, Atmos. Environ. 41 (6) (2007) 1221–1229.
[57] T. Ming, H. Gui, T. Shi, H. Xiong, Y. Wu, Y. Shao, W. Li, X. Lu, R. de Richter, Solar chimney power plant integrated with a photocatalytic reactor to remove atmospheric methane: a numerical analysis, Sol. Energy 226 (2021) 101–111.
[58] T. Ming, H. Xiong, T. Shi, Y. Wu, C. Wang, Y. Wen, W. Li, R. de Richter, N. Zhou, A novel green technology: reducing carbon dioxide and eliminating methane from the atmosphere, Int. J. Energy Res. (2022) 1–14.
[59] M. Serag-Eldin, Mitigating adverse wind effects on flow in solar chimney plants, in: Proceedings of the 4th International Engineering Conference, Sharm El-Sheikh, 2004.
[60] X. Zhou, M.A.d.S. Bernardes, R.M. Ochieng, Influence of atmospheric cross flow on solar updraft tower inflow, Energy 42 (1) (2012) 393–400.
[61] T.Z. Ming, X.J. Wang, R.K. de Richter, W. Liu, T.H. Wu, Y. Pan, Numerical analysis on the influence of ambient crosswind on the performance of solar updraft power plant system, Renew. Sustain. Energy Rev. 16 (8) (2012) 5567–5583.
[62] T.Z. Ming, J.L. Gui, R.K. de Richter, Y. Pan, G.L. Xu, Numerical analysis on the solar updraft power plant system with a blockage, Sol. Energy 98 (-) (2013) 58–69.
[63] T.Z. Ming, Y.J. Wu, R.K. de Richter, W. Liu, S.A. Sherif, Solar updraft power plant system: a brief review and a case study on a new system with radial partition walls in its collector, Renew. Sustain. Energy Rev. 69 (2017) 472–487.
[64] J. Schlaich, The Solar Chimney Edition, Axel Menges, Stuttgart, Germany, 1995.
[65] K. Rahbar, A. Riasi, Performance enhancement and optimization of solar chimney power plant integrated with transparent photovoltaic cells and desalination method, Sustain. Cities Soc. 46 (2019), 101441.
[66] H. Pastohr, O. Kornadt, K. Gurlebeck, Numerical and analytical calculations of the temperature and flow field in the upwind power plant, Int. J. Energy Res. 28 (6) (2004) 495–510.
[67] T.Z. Ming, R.K. de Richter, F.L. Meng, Y. Pan, W. Liu, Chimney shape numerical study for solar chimney power generating systems, Int. J. Energy Res. 37 (4) (2013) 310–322.
[68] A. Haeger, O. Kleinschmidt, D. Hesse, Kinetics of photocatalyzed gas reactions using titanium dioxide as the catalyst part II: photocatalyzed total oxidation of alkanes with oxygen, Chem. Eng. Technol.: Ind. Chem.-Plant Equip.-Proc. Eng.-Biotechnol. 27 (9) (2004) 1019–1026.
[69] X. Wang, X. Tan, T. Yu, Modeling of formaldehyde photocatalytic degradation in a honeycomb monolith reactor using computational fluid dynamics, Ind. Eng. Chem. Res. 53 (48) (2014) 18402–18410.
[70] J.E. Cermak, Applications of fluid mechanics to wind engineering—a freeman scholar lecture, J. Fluid Eng. 97 (1) (1975) 9–38.
[71] W. Haaf, Solar tower, part ii: preliminary test results from the manzanares pilot plant, Sol. Energy 2 (1984) 41–61.
[72] G.L. Xu, T.Z. Ming, Y.A. Pan, F.L. Meng, C. Zhou, Numerical analysis on the performance of solar chimney power plant system, Energy Convers. Manag. 52 (2) (2011) 876–883.
[73] R. Harte, R. Hoffer, W.B. Kratzig, P. Mark, H.J. Niemann, Solar updraft power plants: engineering structures for sustainable energy generation, Eng. Struct. 56 (2013) 1698–1706.
[74] Y. Pratiwi, A. Rejo, A. Fariani, M. Faizal, Source of carbon dioxide emissions equivalent to plant-based control concept with dynamic system in prabumulih city, south sumatra province, IOP Conf. Ser. Earth Environ. Sci. 810 (1) (2021), 012051.
[75] S.K. Guttikunda, P. Jawahar, Atmospheric emissions and pollution from the coal-fired thermal power plants in India, Atmos. Environ. 92 (2014) 449–460.
[76] R. Harte, R. Höffer, W.B. Krätzig, P. Mark, H.-J. Niemann, Solar updraft power plants: engineering structures for sustainable energy generation, Eng. Struct. 56 (2013) 1698–1706. Complete.
[77] W.B. Kratzig, Physics, computer simulation and optimization of thermo-fluidmechanical processes of solar updraft power plants, Sol. Energy 98 (-) (2013) 2–11.
[78] Q.P. Fan, X. Wang, Y.D. Li, Photo-catalytic activity and life time of the TiO2 nano-particles, Chin. J. Inorg. Chem. 19 (5) (2003) 521–526.